Title

Role of Atomic Structure on Exciton Dynamics and Photoluminescence in NIR Emissive InAs/InP/ZnSe Quantum Dots

Journal

The Journal of Physical Chemistry C, 126(17)

ISSN

1932-7447

Authors

Enright, Michael J

Jasrasaria, Dipti

Hanchard, Mathilde M

et al.

Publication Date

2022-05-05

DOI

10.1021/acs.jpcc.2c01499

THE JOURNAL OF PHYSICAL CHEMISTRY C
A JOURNAL OF THE AMERICAN CHEMICAL SOCIETY

pubs.acs.org/JPCC

Article

Role of Atomic Structure on Exciton Dynamics and Photoluminescence in NIR Emissive InAs/InP/ZnSe Quantum Dots

Michael J. Enright,* Dipti Jasrasaria, Mathilde M. Hanchard, David R. Needell, Megan E. Phelan, Daniel Weinberg, Brinn E. McDowell, Haw-Wen Hsiao, Hamidreza Akbari, Matthew Kottwitz, Maggie M. Potter, Joeson Wong, Jian-Min Zuo, Harry A. Atwater, Eran Rabani, and Ralph G. Nuzzo

Cite This: *J. Phys. Chem. C* 2022, 126, 7576−7587

Read Online

ACCESS | Metrics & More | Article Recommendations | Supporting Information

ABSTRACT: The development of bright, near-infrared-emissive quantum dots (QDs) is a necessary requirement for the realization of important new classes of technology. Specifically, there exist significant needs for brighter, heavy metal-free, near-infrared (NIR) QDs for applications with high radiative efficiency that span diverse applications, including down-conversion emitters for high-performance luminescent solar concentrators. We use a combination of theoretical and experimental approaches to synthesize bright, NIR luminescent InAs/InP/ZnSe QDs and elucidate fundamental material attributes that remain obstacles for development of near-unity NIR QD luminophores. First, using Monte Carlo ray tracing, we identify the atomic and electronic structural attributes of InAs core/shell, NIR emitters, whose luminescence properties can be tailored by synthetic design to match most beneficially those of high-performance, single-band-gap photovoltaic devices based on important semiconductor materials, such Si or GaAs. Second, we synthesize InAs/InP/ZnSe QDs based on the optical attributes found to maximize LSC performance and develop methods to improve the emissive qualities of NIR emitters with large, tunable Stokes ratios, narrow emission linewidths, and high luminescence quantum yields (here reaching 60 ± 2%). Third, we employ atomistic electronic structure calculations to explore charge carrier behavior at the nanoscale affected by interfacial atomic structures and find that significant exciton occupation of the InP shell occurs in most cases despite the InAs/InP type I bulk band alignment. Furthermore, the density of the valence band maximum state extends anisotropically through the (111) crystal planes to the terminal InP surfaces/interfaces, indicating that surface defects, such as unpassivated phosphorus dangling bonds, located on the (111) facets play an outsized role in disrupting the valence band maximum and quenching photoluminescence.

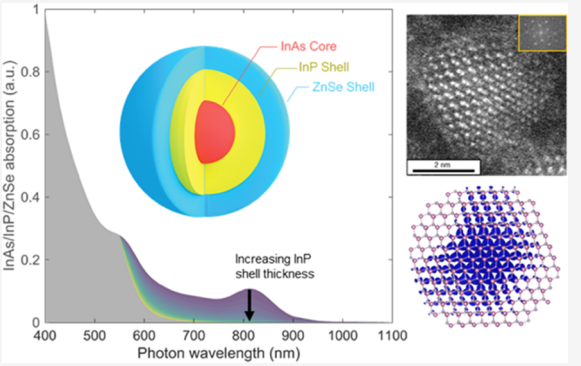

INTRODUCTION

A substantial body of research over several decades has led to the development of colloidal quantum dots (QDs) with optoelectronic properties in the ultraviolet (UV) and visible regions of the electromagnetic spectrum, which in turn has led to remarkable advancements that include new commercial technologies.[1−7] QDs with near-infrared (NIR, 750−1400 nm) emission have not yet attained the same utility despite exceptional promise across a wide spectrum of applications as they are uniquely suited for use in photovoltaic energy conversion, luminescence concentration, telecommunications, and in vivo imaging among other applications.[2,6−12] Advancement of technologies based on NIR QD materials has been challenging for reasons that are physicochemical in nature due to the limited number of semiconductor materials that exist with useful, easily tunable optical properties at NIR frequencies, which has frustrated their development as compared to their UV and visible counterparts.[2,4,6−15] It also remains a specific and urgent need to provide new QD material systems that are both cadmium- and lead-free, yet still afford NIR capabilities such as high fluorescence quantum yields, stability against photodegradation, and narrow emission profiles.[16−23] Realization of new QDs with these attributes are a prerequisite for development of high-performance technologies.

Luminescent solar concentrators (LSCs), which have the potential to revolutionize solar collection in urban environments, operate by collecting direct and diffuse solar radiation over a large area and concentrating that energy into a narrow output region, ideally, one matched with the band gap of a solar cell, by luminescence. More specifically, the benefits of

Received: March 2, 2022
Revised: March 21, 2022
Published: April 26, 2022

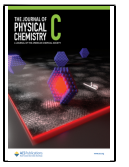

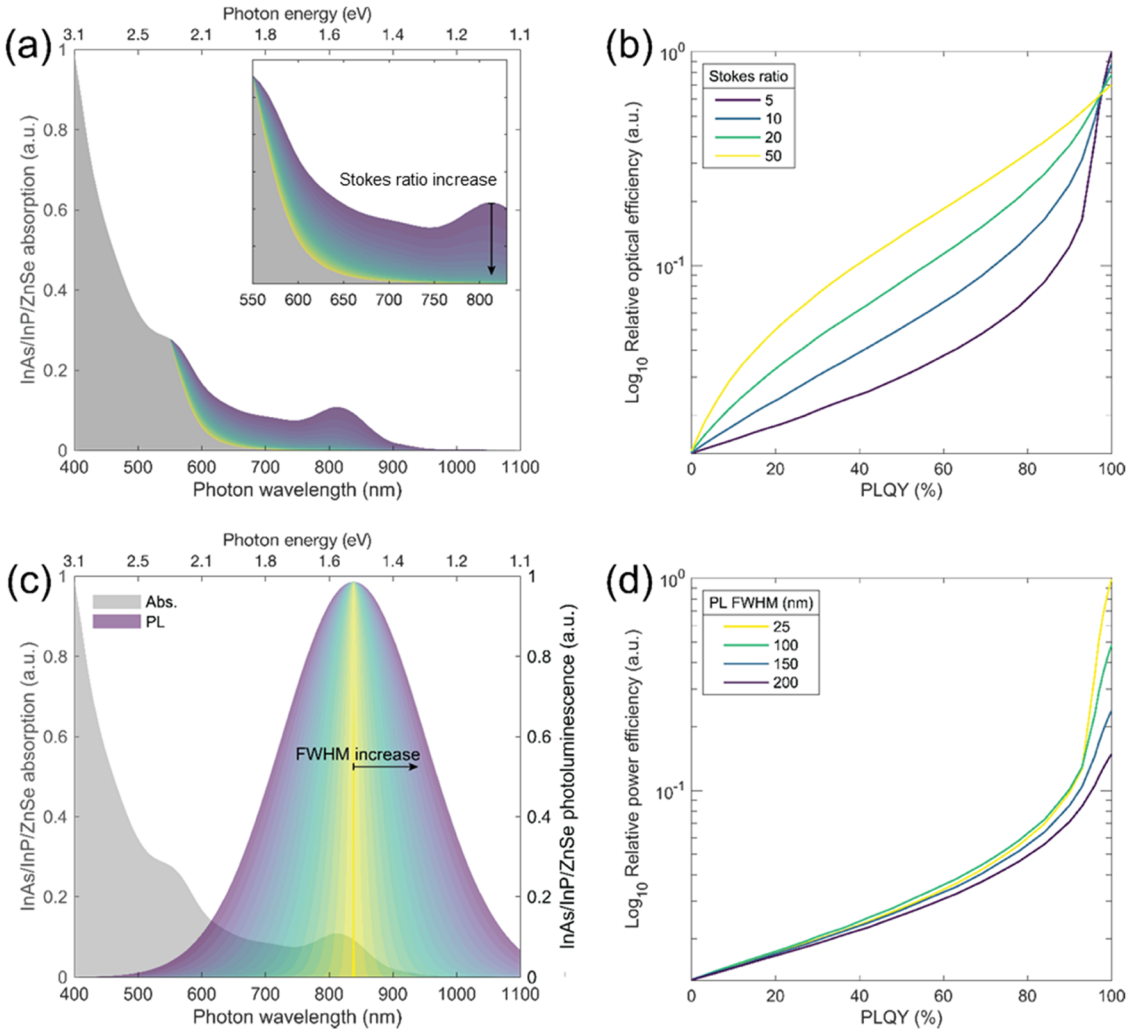

Figure 1. Monte Carlo simulations of the impact of synthetically tunable optical properties of NIR emissive InAs/InP/ZnS on luminophore performance in LSCs. Absorption and emission profiles of QDs are based on experimentally derived InAs/InP/ZnSe QDs, as described in the Methods Section. The Stokes ratio-modified absorbance profile (a) uses a fixed absorption in the visible region at 550 nm across variable NIR absorption from InAs cores where the Stokes ratio increases from violet to yellow. The inset highlights the increased Stokes ratio with decreasing NIR absorption. A fixed optical density in the visible region enables a comparison of the relative waveguide optical efficiency across the Stokes ratio (b). Variable emission full width at half maximum (FWHM) increases from yellow to violet about a fixed emission maximum (c). Monodisperse QDs give narrower FWHM and decrease losses below the solar cell band edge and improve module efficiency (d). Optical and power efficiencies improve exponentially with PLQY, with more than 5-fold increases in optical and power efficiencies between 90 and 100% PLQY. A logarithmic scale is applied to highlight the impacts of the Stokes ratio and FWHM on LSC efficiencies at <90% PLQY. An absolute short-circuit current density and power efficiency are reported in Figure S1. Relative optical and power efficiencies are reported compared to an overall highest theoretical efficiency for any Stokes ratio or photoluminescence FWHM. Across all simulations, the module performance increases from violet to yellow traces.

LSCs with a broad absorption band provided by an NIR luminophore can, in principle, be simultaneously maximized for direct and diffuse light harvesting across the visible region of the solar spectrum while providing a fluorescence output well matched with the band gap of the coupled solar cell. To do so, an optimal LSC requires luminophores with large Stokes ratios and narrow NIR emission to minimize losses from parasitic reabsorption and emission below the band gap of a solar collector.[12,24−26] In this work, the Stokes ratio is defined as the ratio of absorbance at 550 nm to the maximum extinction in the NIR that overlaps with the luminescence profile.

Among candidate semiconductor materials, indium arsenide (InAs) offers potential advantages as a central core for QDs with NIR optical gaps. Most notable is the body of the prior work that demonstrates good prospects for developing InAs-based QDs offering higher photoluminescence quantum yields (PLQYs) than other comparable NIR materials, including rare earth nanocrystals, silver chalcogenide nanocrystals, carbon nanotubes, Si nanoparticles, and organic dyes.[27−32] Unshelled, InAs cores have very low PLQYs—typically less than 2% due to rapid surface trapping of charges from poor surface passivation and states resulting from surface oxidation. These impacts can be remediated in part by encapsulation of the InAs core within a wide-band-gap, epitaxial shell material. Effective shell phases narrow emission linewidths and increase radiative recombination efficiencies through charge carrier confinement and passivation of the InAs core.[33−35] With few exceptions, the highest PLQY InAs QDs described in the current literature are ones passivated by cadmium chalcogenide (CdSe or CdS)

https://doi.org/10.1021/acs.jpcc.2c01499
J. Phys. Chem. C 2022, 126, 7576−7587

protective shells, with luminescence quantum yields in excess of 80% being reported.[36] The increased brightness is often accompanied by large bathochromic shifts, which are changes in the spectral band position toward longer wavelengths, of several hundred meV that can push the emission band beyond the band gap of a solar cell.[11,34,36,37] These shifts are a confluence of both the extension of the excitonic wavefunction into the shell and cation exchange between cadmium and indium to give cadmium pnictide products, thereby posing a challenge to the heterostructure development needed for technologies that require operation within a narrow emission range.[38,39]

Here, we examine InAs/InP/ZnSe QDs—heavy-metal-free, core/multishell heterostructure luminophores with exceptional promise for utilization as active absorber/emitter materials in high-performance LSCs for photovoltaic energy conversion. The necessary improvements in material properties are well illustrated in the Monte Carlo ray-tracing simulations of InAs/InP/ZnSe QDs in LSCs, which are shown in Figure 1. Here, we calculate expected LSC performance parameters based on explicit tunable luminophore characteristics, including QD brightness, Stokes ratio, and emission full width at half-maximum (FWHM). As the simulations demonstrate, high PLQY QDs with increased Stokes ratios and narrow FWHM have the potential to greatly improve luminophore performance and LSC solar conversion efficiency. Both optical efficiency (the fraction of photons retained within a waveguide) and solar conversion efficiency (overall LSC light-harvesting performance including a solar cell) improve exponentially with increases in the PLQY.

Even without near-unity PLQY, increasing the Stokes ratio and narrowing emission FWHM significantly improve the module optical efficiency and power efficiency, respectively. Regarding the former, Figure 1a simulates the absorbance spectra of QDs with a constant optical density in the visible region up to 550 nm with progressively decreasing NIR light absorption. These spectra simulate an increased Stokes ratio representative of the optical properties achieved through increasing InP shell thickness synthetically. The optical efficiencies of LSC waveguides so tuned are seen to improve markedly with increases in the Stokes ratio (Figure 1b). The FWHM, valuable for limiting the number of photons re-emitted with energies below the band gap of the solar harvester, is strongly impacted by the mass distribution (i.e., monodispersity) of the QDs. Figure 1c shows illustrative simulations using the emission spectra of QDs with variable FWHM at a fixed emission maximum wavelength to demonstrate this point. Narrow FWHM, especially at high PLQY, is essential to maximize the LSC module power efficiency, which includes the absorption profile of GaAs and Si solar cells (Figures 1d and S1). For example, at <80% PLQY, the benefits from reduced parasitic reabsorption at a longer wavelength below the absorbance profile for wide FWHM offset the losses from photons emitted below the solar cell band gap. As the PLQY increases and parasitic reabsorption is no longer the primary loss mechanism, narrow emission leads to significant increases in LSC performance. High Stokes ratios greatly enhance the optical efficiency by reducing parasitic reabsorption and bolster LSC efficiencies most significantly at low PLQY, while narrow FWHM reduces sub-band-gap losses at the solar cell and yields the highest gains at high PLQY. Narrow FWHM, high Stokes ratios, and >90% PLQY NIR QD luminophores are essential requirements for a high-efficiency LSC-PV technology.

To date, only visibly emissive QDs have been successfully developed to these standards. Notably, CdSe/CdS QDs with >95% PLQY, Stokes ratios >30 (defined by Bronstein et al. as the ratio of absorption at 450 nm to the extinction at the peak luminescence wavelength),[40] and emission linewidths around 100 meV are the gold standard for the brightest QD emitters.[41,42] The encapsulation of III−V QDs within wide-band-gap II−VI shells has yielded a second, structurally distinct class with >80% PLQYs reported for InP/ZnSe and InP/ZnSeS.[43−45] Taken together with Figure 1, such metrics would enable exceptional LSC performance if matched by NIR QDs, though these same levels of broadly tunable photophysical performance needed from NIR emitters to support high PCE LSC-PV technologies are not yet developed. For the InAs-shelled QDs of interest in the current work, this is primarily due to the large lattice mismatches between InAs and prospective wide-band-gap protective ZnSe (6.4%) and ZnS (10.7%) shells that limit defect-free growth of these layers to only a few monolayers at most.[20,34] Studies investigating the incorporation of multiple intermediate layers and alloys to relieve strain and facilitate thicker ZnSe or ZnS shell growth (e.g., the continuous-injection synthesis of InAs/In(Zn)P/ZnSe/ZnS and InAs/InZnP/GaP/ZnSe with a gradient composition GaP shell), yielded emitters with only modest PL quantum efficiencies (25 and 23%, respectively).[34,46] Further efforts using an alloyed core and a large interior shell obtained 75% PLQY for In(Zn)As/In(Zn)P/GaP/ZnS QDs.[47] Bright, NIR emissive InAs/InP/ZnSe QDs with 76% PLQY have also been reported, though the specific structural and electronic attributes that enable bright quantum yields are not yet understood, especially when contrasted with the <30% PLQYs typically observed InAs/InP/ZnSe QDs.[48] Here, we explore the relationship between the QD structure, synthesis, and performance and highlight specific synthetic interventions that lead to improvements in PLQY for a more direct comparison of QDs across PLQY.

The current work employs a combination of experimental and computational strategies to develop a deeper understanding of the atomic-scale structural and electronic properties that enable (or inhibit) NIR emission in these QD heterostructures. Synthetically, we developed replicable methods for the synthesis of InAs/InP/ZnSe QDs with quantum yields of up to 60 ± 2% and emission full width at half-maximum (FWHM) as narrow as 130 meV with tunable Stokes ratios and emission between 800 and 900 nm. Atomistic electronic structure calculations of InAs/InP QDs indicate that charge carriers in these materials are poorly confined to the InAs core, despite the nested, type I band structure of the bulk materials (Figure S2). We find that the electron wavefunction extends isotropically into the shell but remains close to the InAs/InP interface. The hole, however, delocalizes anisotropically into the InP layer primarily in the [111] direction. Atomically resolved microscopy of InAs/InP/ZnSe QDs reveals that the growth process is strongly anisotropic, leading to a shell encapsulation that is nonuniform (even in the brightest samples) and thinner in the [111] direction. An accompanying theoretical assessment of InP surface defects shows that the extent of overlap between surface defect states and the QD valence band states is orientation-dependent, such that defects located along the ⟨111⟩ axes play an outsized role

https://doi.org/10.1021/acs.jpcc.2c01499
J. Phys. Chem. C 2022, 126, 7576−7587

in influencing the QD band structure, while defects elsewhere are surprisingly found to have almost no impact.

METHODS

Materials. All glassware was dried in an oven overnight at 160 °C before use. All manipulations were performed using standard Schlenk or glovebox techniques under dry N_2. Indium(III) acetate ($In(Ac)_3$, 99.99%), zinc undecylenate (98%), selenium (Se, 99.999%), trioctylphosphine (TOP, 97%), stearic acid (95%), and tris(trimethylsilyl)phosphine ($P(SiMe_3)_3$, 95%) were purchased from Sigma-Aldrich and used as received without further purification. Zinc 2-ethylhexanoate (Zn ≈ 20%, cont. 1% diethylene glycolmonomethyl ether) was purchased from Fisher Scientific and used as received. 1-Octadecene (1-ODE, 90%) and octylamine (99.5%) were purchased from Sigma-Aldrich and distilled and stored over 3 Å molecular sieves prior to use. Anhydrous ethanol, ethyl acetate, and toluene were obtained from Sigma-Aldrich and used as received. Tris(trimethylsilyl)arsine ($As(SiMe_3)_3$) was synthesized as reported previously.[49]

Synthesis of InAs/InP/ZnSe QDs. The synthesis of InAs/InP/ZnSe was modified from several previous reports on InAs core/shell QDs.[36,46,48,50] A typical synthesis of InAs/InP/ZnSe began with 0.4 mmol of indium stearate prepared in situ by degassing 0.117 g (0.4 mmol) of $In(Ac)_3$, 0.341 g (1.2 mmol) of stearic acid, and 3.5 mL of 1-ODE at 120 °C under vacuum for at least 2.5 h in a 50 mL, three-neck round bottom flask. The mixture was heated to 300 °C under nitrogen until clear to form indium stearate before being cooled to 230 °C, the QD reaction temperature. Upon reaching the reaction temperature, 0.5 mL of TOP was added and the temperature is allowed to restabilize at 230 °C. A solution of 17.1 μL (0.05 mmol) of $As(SiMe_3)_3$ and 2 mL of ODE was rapidly injected to seed and grow InAs QDs. After 20 min, InAs QDs with 2.7 ± 0.2 nm diameters were obtained and the reaction was temporarily removed from the heat to cool to 178 °C. We found that replacing the heating mantle when the reaction temperature was 185 °C helped stabilize the temperature at 178 °C more quickly while also enabling rapid cooling between core and shell growth.

When the reaction temperature reached 178 °C, a solution of 58.1 μL (0.2 mmol) of $P(SiMe_3)_3$, 0.162 mL of octylamine (1 mmol), and 0.8 mL of 1-ODE was rapidly injected to begin InP shell growth. For larger InAs QDs (>3.0 nm), the QDs become heterogeneous during subsequent shell growth steps, so 0.085 g (0.3 mmol) of stearic acid in 0.5 mL of ODE, prepared by heating at 60 °C, was added at 110 °C prior to elevating the temperature to 178 °C for phosphorus precursor addition. InP growth proceeded for 45 min. Thicker-shelled InP QDs (>1 nm thick) were obtained through additional injections of phosphorus and indium stearate (prepared as described above) with subsequent additions of phosphorus and indium precursors supplied 30 min after the first addition of $P(SiMe_3)_3$ solution. Subsequent additions exceeding 0.2 mmol of phosphorus or indium led to independent nucleation of new InP QDs. Then, 45 min after the final indium and phosphorus additions, the temperature was increased to 220 °C for ZnSe shell encapsulation. QDs with 60 ± 2% PLQY were obtained from syntheses with only a single phosphorus and indium addition. Thicker InP-shelled QDs, shown in Figures S3 and S4, included a second addition of phosphorus and indium as described and the brightest QDs obtained this way had 51 ± 2% PLQY.

At 220 °C, 0.4 mmol of zinc 2-ethylhexanoate was added to the reaction vessel. After 2 min, 0.2 M TOP-Se was added in three additions of 0.04 mmol of Se (0.2 mL), 0.06 mmol (0.3 mL), and 0.08 mmol (0.4 mL) in 30 min increments. With each subsequent addition, the temperature is raised 10 °C and the reaction is quenched by removing the heat 30 min after the final addition of TOP-Se. QDs are purified by multiple precipitations in ethanol and resuspension in toluene. Inclusion of 5−10 mL of ethyl acetate in the initial precipitation cycle assists in the removal of excess 1-ODE and assists nanoparticle precipitation. QDs with 60 ± 2% PLQY were obtained after five precipitations and resuspension cycles. The QDs reported in Figure S5 used 0.4 mmol of zinc undecylenate in 2 mL of ODE instead of zinc 2-ethylhexanoate and gave QDs with 39 ± 3% PLQY.

Characterization. UV−vis absorption spectra were obtained using a Varian Cary 5G spectrophotometer, and fluorescence measurements were acquired on a home-built spectrometer using 532 nm CW and Ti:Sapphire emission sources with a CCD camera detector. The same system was used for PLQY measurements, and all measurements are reported at the 95% confidence limit. Time-resolved photoluminescence was acquired on a home-built spectrometer with a supercontinuum fiber laser with a pulse width of 6 ps and a Si single-photon counting avalanche photodiode (SPC-APD) detector. Biexponential fit parameters were used to evaluate exciton decay times. A PerkinElmer Optima 8300 inductively coupled plasma−optical emission spectrophotometer was used for elemental analysis and was performed by the Microanalysis Laboratory of the UIUC School of Chemical Sciences. STEM images were obtained on an FEI Themis Z Advanced Probe aberration-corrected analytical microscope. Analysis of STEM images was performed using ImageJ software. Powder X-ray diffraction data were recorded on a Bruker D8 Advance instrument with an Eiger2 R 500K 2D detector.

Monte Carlo Simulations. The Monte Carlo ray trace model stochastically traces individual photons through a rectangular, optically thick (200 μm) waveguide of an arbitrary medium with a real index of refraction of 1.5 assumed for all photoluminescence wavelengths. To ensure proper statistical reliability, we initialized a grid matrix across the waveguide top surface area of 4 mm × 4 mm that, for each wavelength of incident light, injects over 20,000 photons into the luminescent solar concentrator device. The device itself consists of a top glass layer of 50 μm, a waveguide layer doped with InAs/InP/ZnSe quantum dot luminophores, and a bottom glass layer of 50 μm. Given the absorption/emission spectra of the luminophores and optically coupled solar cells, we simulate photon wavelengths between 300 and 1200 nm in steps of 10 nm. Therefore, following previously reported Monte Carlo methods, we modeled over 2×10^6 photons for each model variation (i.e., for a specific InAs/InP/ZnSe quantum dot spectra).[51,52] Additional details about Monte Carlo simulations, including model validation, are included in the Supporting Information.

InAs/InP Electronic Structure Calculations. To perform atomistic electronic structure calculations on InAs/InP core/shell quantum dots (QDs), we developed a model within the semiempirical pseudopotential method that involves fitting a single pseudopotential each for In, As, and P that reproduces accurate band structures for both bulk InAs and bulk InP.[53,54] The filter-diagonalization technique was used to obtain quasiparticle states from the single-particle Hamiltonian.[55]

https://doi.org/10.1021/acs.jpcc.2c01499
J. Phys. Chem. C 2022, 126, 7576−7587

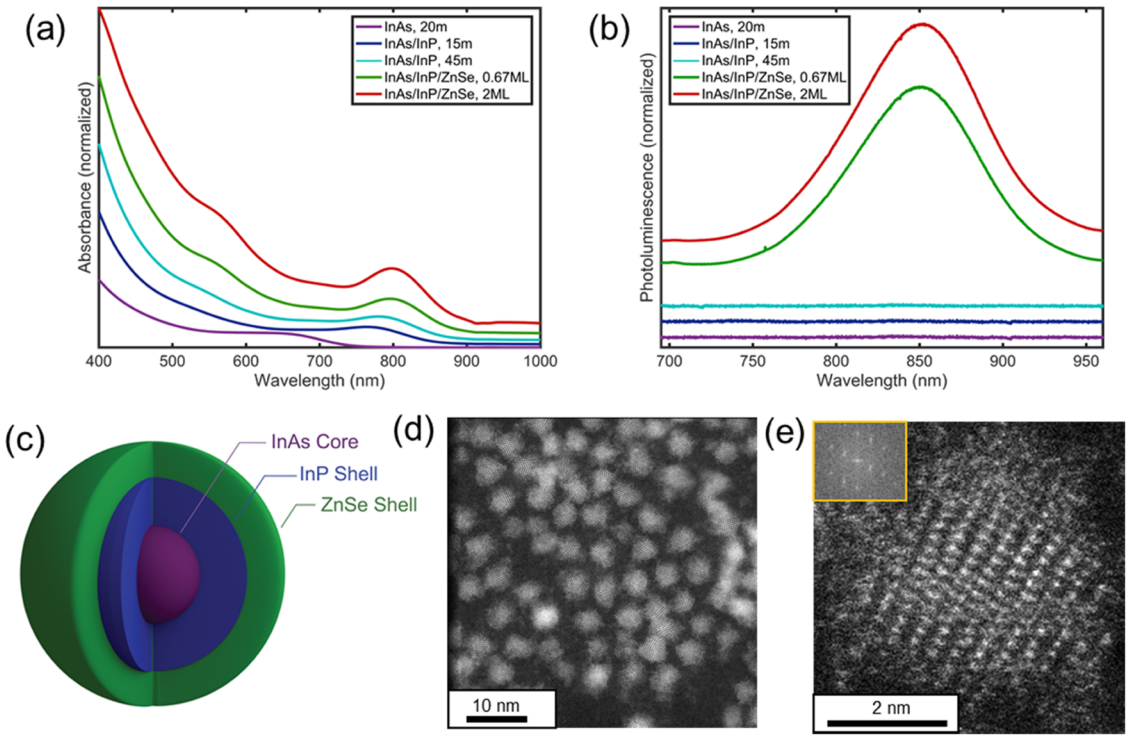

Figure 2. Synthesis of InAs/InP/ZnSe quantum dots with 1 nm thick InP and 2 ML thick ZnSe shells monitored by intermittent extractions over the course of the reaction. The evolving absorbance (a) and photoluminescence (b) of the quantum dots show an initial bathochromic shift by almost 100 nm upon initial growth of the InP shell followed by sharpening of absorbance features from the InAs core and InP shell when encapsulated within ZnSe. Photoluminescence is not observed until particles are treated with ZnSe. A depiction of a spherical, core/multishell, InAs/InP/ZnSe QD (c) is accompanied by transmission electron micrographs of InAs/InP/ZnSe with 1 nm thick InP shells and a 10 nm scale bar (d) and an atomically resolved QD observed from the (211) plane with a 2 nm scale bar, and the inset of the power spectrum indicating the (211) zone axis (e).

The Bethe−Salpeter equation was then solved to obtain correlated electron−hole pair (i.e., excitonic) states.[56] Calculations were performed on fully passivated QD structures relaxed using molecular dynamics-based geometry minimization.[57,58] Hole trap states were modeled by the removal of a passivation ligand from a surface phosphorus atom. Additional details are included in the Supporting Information and in Table S1 and Figures S6 and S7.

RESULTS AND DISCUSSION

InAs/InP/ZnSe core/multishell QDs are prepared in a three-step process where InAs cores are nucleated by hot injection followed by epitaxial growth of InP and ZnSe shells. Representative QDs with InAs cores between 2.5 and 3.3 nm were synthesized using indium stearate and (trimethylsilyl)-arsine as source compounds. The size of the InAs core can be modified through modulation of both the growth time and temperature and ultimately dictates the emissive properties (albeit low, <1% PLQY) of the nascent heterostructure before shelling (Figure S8). The InP shell growth is carried out at 178 °C, a lower temperature than required for growth of the InAs core, to inhibit nucleation of InP QDs. The brightest QDs with quantum yields of 60 ± 2% are encapsulated with ZnSe via additions of trioctylphosphine selenide and zinc 2-ethylhexanoate (2:1 zinc to selenium).

The evolving optical properties of the reaction mixture were followed by absorbance and photoluminescence spectroscopy and accompanied by high-angle annular dark-field−scanning transmission electron microscopy (HAADF−STEM) images of the final multishell QDs to ascertain their atomic structure, as shown in Figure 2. The progression of photophysical/spectroscopic properties through an illustrative sequence of growth stages is shown in Figure 2a,b. Encapsulation within InP and ZnSe both lead to bathochromic shifts in the lowest energy excitonic transition in the absorbance spectra. Emission is extremely weak or not detected throughout InP shell growth but becomes pronounced upon ZnSe encapsulation (an impact that is marked even without a complete ZnSe monolayer). Ideally, the indicated sequences would lead to the schematic core/multishell structure shown in Figure 2c. Representative STEM data shown in Figure 2d,e illustrate the high level of atomic order present in the InAs/InP/ZnSe QDs that are formed, as evidenced by the representative (211) zone axis projection shown in the inset of Figure 2e.

The InP shell thickness is controlled using a successive ionic layer adsorption and reaction (SILAR) approach that enables the realization of tunable Stokes ratios over a range of nearly an order of magnitude, from as low as 1.5 up to 8.5 as depicted in the absorbance spectra in Figures S3 and S8 and calculated from the absorbance ratio at 550 nm vs absorbance at the lowest energy excitonic transition. Increasing the InP shell thickness but omitting the ZnSe shell, however, yields invariably weakly luminescent heterostructures (<1% PLQY). As noted above, STEM data (shown in Figures 2d and S5) reveal that the progression of shell growth is associated with the formation of increasingly anisotropic (tetrahedral-like) heterostructures. The phenomenon of zinc blende crystal structures (as illustrated by X-ray diffraction data given in Figure S9) with a slightly tetrahedral shape has been observed previously for the growth of InAs/InP QD materials.[38,46,59] At

https://doi.org/10.1021/acs.jpcc.2c01499
J. Phys. Chem. C 2022, 126, 7576−7587

the termination of the InP shell growth (as observed by an unchanging UV−visible absorbance profile), subsequent encapsulation with ZnSe can be affected to give highly emissive InAs/InP/ZnSe particles—QDs with 60 ± 2% PLQY and a narrow emission FWHM of 132 meV.

We note here that the structures realized are highly sensitive to even modest modifications made in the growth conditions, and we found that the optimal synthetic route to usefully emissive InAs/InP/ZnSe materials follows from a SILAR-type growth of the ZnSe shell. This is illustrated in a comparison of the results of various ZnSe shell growth approaches, as given in Figure S5, and comparisons to previous investigations in Figure S10.[37,46,48,60] Notably, we find that shell growth via dropwise precursor addition (a method extensively reported for the growth of III−V material QD systems) leads to markedly anisotropic shell growth. This phenomenon is most pronounced in syntheses targeting thicker shells, as shown in Figure S4 and corroborated by the results of prior investigations.[34,36,46,61] Further improvements to PLQY were obtained using zinc 2-ethylhexanoate to achieve QDs with 60 ± 2% PLQY, as depicted in Figure S11.

The optimized sequence of growth steps outlined in Figure 2 yields QDs with large but still far from unity values of PLQY. Their tunable emission bands have relatively narrow FWHM. When taken together, there remains a clear opportunity to better the performance of these and related materials to meet the most demanding requirements of NIR luminophores for applications in technology. Theoretical investigations based on and extending from the current data provide a means to bridge the gap in the current understanding of the atomic and electronic features of the structure that underpin performance in this case.

While the nested type I bulk band alignment would suggest that InAs/InP/ZnSe QDs could give bright NIR emitters, strong quantum confinement of carriers in InAs and InP QDs complicates this oversimplified picture. To better understand the properties of these nanostructures, we performed atomistic electronic structure calculations on InAs/InP QDs of experimentally relevant sizes. Exterior ZnSe shells used as passivation layers experimentally are modeled as ligand potentials in the simulated InAs/InP QDs. Exploration of defects at an InP/ZnSe interface from an incomplete ZnSe shell are modeled through the creation of phosphorus dangling bonds at the InP surface. Calculations were performed within the semiempirical pseudopotential method to obtain quasiparticle (electron and hole) states at the conduction and valence band edges.[53,55,62] These quasiparticle states were used as input to the Bethe−Salpeter equation, which was solved to obtain correlated electron−hole pair (i.e., excitonic) states.[56] Details of the pseudopotential parameterization and other computational methods are provided in the Supporting Information.

The projected electron and hole carrier densities for the ground excitonic state of a 2.5 nm InAs QD with a 1.1 nm InP shell are depicted in Figure 3a. Despite conventional wisdom that the type I band alignment of InAs/InP would confine carriers to the core, both the electron and hole are delocalized throughout the QDs with 53.8 and 26.5% of the electron and hole densities, respectively, in the shell.[63] Unsurprisingly, the electron is more delocalized than the hole due to its lighter effective mass. These results are indicative of InAs/InP nanostructures having a quasi-type II band structure as opposed to the type I band structure present in bulk

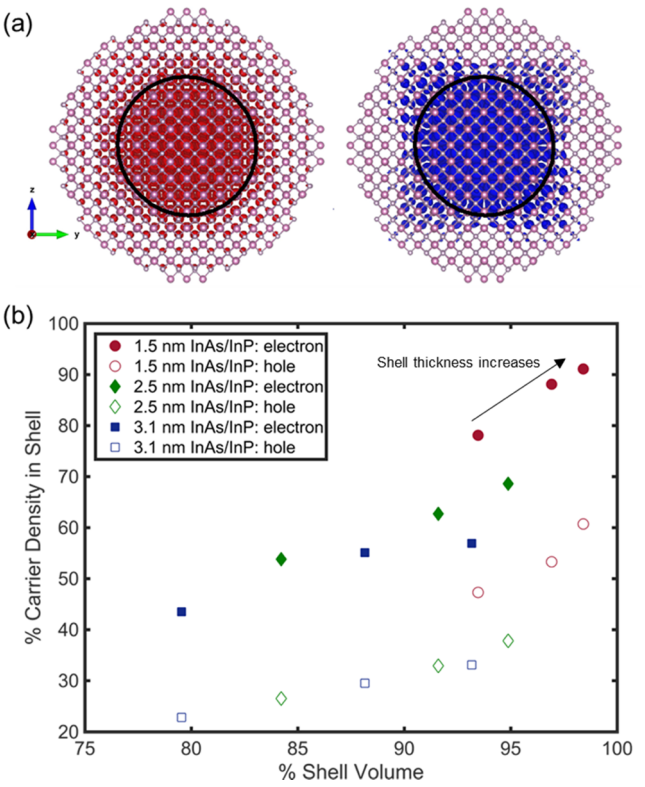

Figure 3. Projected densities of the electron (red) and hole (blue) of the ground state exciton of an InAs/InP QD with a 2.5 nm diameter InAs core with a 1.1 nm InP shell (a). As the relative shell volume of structures increases with thicker shells, the percentage of the carrier density in the shell increases for both electrons and holes (b). Charge carrier densities are views along the (100) zone axis. Electrons have higher shell occupancy than holes but remain isotopically localized near the core/shell interface while holes will delocalize to the shell at lower probabilities but extend anisotropically and further toward the surface. The percent shell volume is defined as the volume of the shell over the total QD volume. Core/shell dimensions are noted explicitly in Table S2.

materials.[46] Figure 3b shows that carrier occupancy of the shell increases with both decreasing InAs core size and increasing InP shell thickness. Projected band edge densities and carrier delocalization maps of a series of InAs/InP particles of different core and shell sizes are depicted in Figures S12 and S13. This delocalization is attributed to the large exciton Bohr radii in InAs and InP, which are 34 and 15 nm, respectively, indicating that the carriers on the QDs are strongly quantum confined and have sufficient kinetic energies to tunnel through the confining potential created by the InAs−InP band offset and into the shell.[64] The electron−hole interactions are not strong enough to overcome the strong quantum confinement and localize the carriers to the InAs core.

Our calculations demonstrate that the electron in the ground state exciton tunnels isotropically into the shell. The hole, however, exhibits a facet-dependent delocalization into the InP shell through the (111) facets. Growth of an InP shell causes compression of the InAs core, as shown by molecular dynamics-based geometry optimization illustrated in Figure S14, which causes the InAs valence band maximum (VBM) to decrease in energy. This VBM energy decrease has been shown to be a facet-dependent effect that locally decreases the InAs/InP valence band offset most significantly along the (111) facets, permitting tunneling of the hole wavefunction in those

https://doi.org/10.1021/acs.jpcc.2c01499
J. Phys. Chem. C 2022, 126, 7576−7587

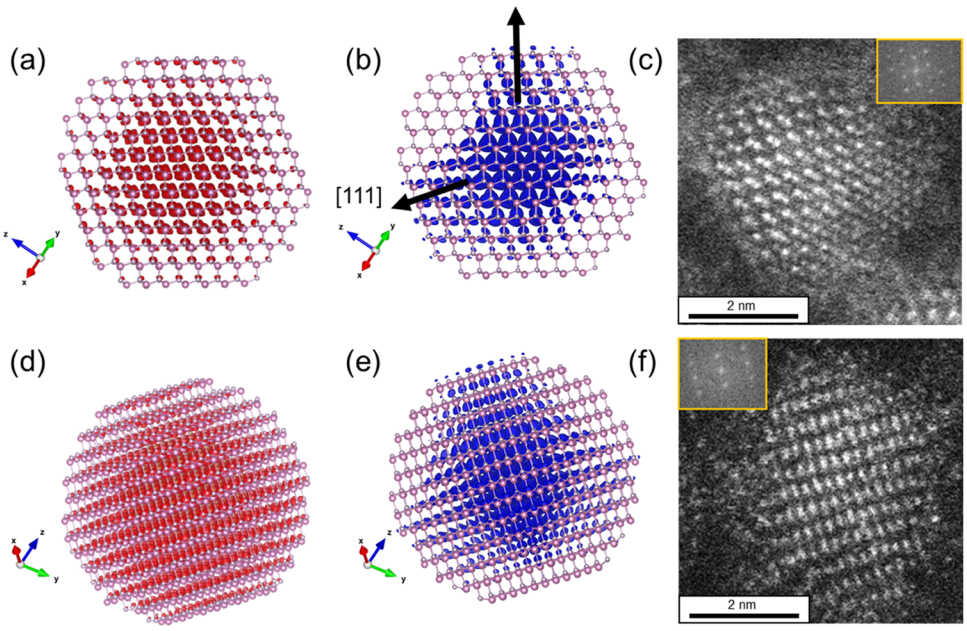

Figure 4. Projected density of the exciton electron (red, a) and hole (blue, b) of an InAs/InP QD with a 2.5 nm core and 1.1 nm InP shell as viewed from the (110) orientation matched to similarly aligned atomically resolved TEM image of a single InAs/InP/ZnSe QD with a 2 nm scale bar and power function inset (c). An alternately oriented view of the electron (red, d) and hole (blue, e) displayed from the (111) orientation matched to similarly aligned atomically resolved TEM image of a single InAs/InP/ZnSe QD with a 2 nm scale bar and power function inset (f). The electron density is relatively isotropic and delocalized, while the hole density extends into the InP shell via the [111] direction. Arrows indicating the [111] vectors are in plane with the projections.

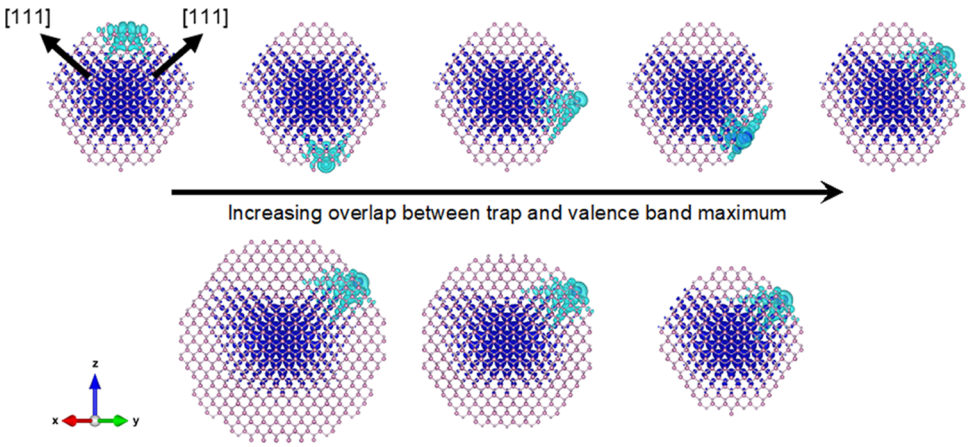

Figure 5. Trends of the density overlap between a quasiparticle surface defect state (cyan) and the quasiparticle VBM (blue) for defects located at the surface of InAs/InP QDs. The series on the top depicts a 2.5 nm InAs core and 1.1 nm InP shell QD with surface traps on different facets while the series on the bottom illustrates a 2.5 nm InAs core with InP shell thicknesses of 2.2, 1.6, and 1.1 nm. Arrows indicating the [111] vectors are in plane with the projections. There is an increasing overlap between the surface trap state and the VBM when the defect is centered on a (111) facet and directly aligned with the delocalization of the VBM into the shell. Defects located away from the (111) facets have diminished interaction with the VBM such that when the defect is aligned directly away from the axis of hole delocalization (two QDs in the upper left), there is a negligible defect-VBM overlap. Similarly, increasing the shell thickness reduces the overlap between surface defects and the VBM.

directions.[65,66] Comparing these observations with atomically resolved STEM images in Figures 4 and S15, we have identified that the axes with a greater hole density correspond to directions of the narrowest radius in the synthesized QDs. Figure 4a,b depicts the projected density of an excitonic hole from the (110) orientation. From this orientation, delocalization in the ⟨111⟩ directions to the surface is straightforwardly observed. The extent of charge carrier delocalization to the InP shell suggests that the InP shells do a poor job of confining charge carriers to the InAs core and indicates that the InP/ZnSe interface is particularly important for exciton confinement. When taken together with Figure 4c, an atomically resolved STEM image of an identically oriented QD, the directions of hole delocalization align with directions of shorter radii in the slightly asymmetric, synthesized nanocrystals. Figure 4d,e depict the projected excitonic hole density as viewed from the (111) orientation where tetrapodal, anisotropic delocalization into the shell is readily observed with a hole density from one of the [111] axes projecting perpendicular to the plane of view. The accompanying Figure 4f shares the same (111) orientation, as is confirmed by the inset of the power function. The matched electronic structure

https://doi.org/10.1021/acs.jpcc.2c01499
J. Phys. Chem. C 2022, 126, 7576−7587

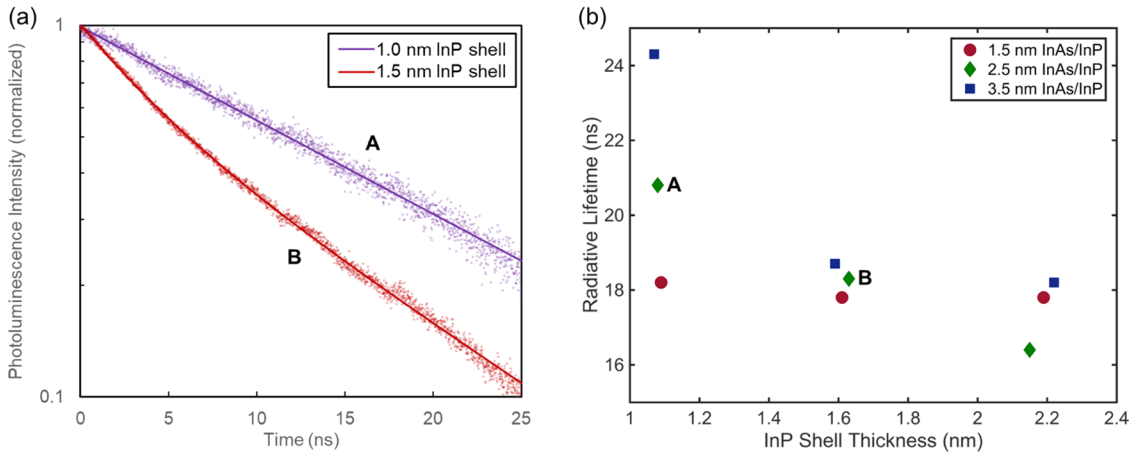

Figure 6. Exciton decay lifetimes of InAs/InP/ZnSe QDs. Photoluminescence decay curves of the InAs/InP/ZnSe QDs with 2.7 ± 0.2 nm InAs cores and 1.0 ± 0.1 (violet) or 1.5 ± 0.1 nm (red) thick InP shells with 3 ML thick ZnSe shells fitted with monoexponential decays (a). Calculated radiative lifetimes for InAs/InP across a spectrum of InAs core sizes (indicated in legend) and InP shell thicknesses (*x*-axis) shows a correlation between thicker InP shells and shorter radiative lifetimes (b). The InAs core and InP shell sizes of the QDs annotated **A** and **B** between the TRPL decay curves from panel (a) and calculated radiative lifetimes from panel (b) share similar sizes and highlight the decreasing trend between the radiative lifetime and shell thickness. Despite challenges associated with synthesizing high PLQY InAs/InP/ZnSe QDs with variable InAs and InP sizes, these calculations suggest that the observed decrease in decay time for 2.7 ± 0.2 nm InAs core QDs would extend across the QD core size and InP shell thickness. The exciton decay curves of <1 ML ZnSe-shelled QDs is shown in Figure S18.

calculations and atomically resolved STEM images highlight the importance of uniform InP and ZnSe passivation to insulate excitons and mitigate deleterious outcomes from holes delocalizing to passivated surfaces.

Due to delocalization of the ground state exciton out of the InAs core, defects at the InP/ZnSe interface may have a significant impact on the particle's optical properties. Prior work on highly emissive InP cores with ZnSe shells observed nonuniform shell growth caused by oxidation of surface indium and phosphorus to create $InPO_x$ and In_2O_3 defects during synthesis.[67] Oxidized phosphorus present at InP/ZnSe interfaces is known to form deep trap sites.[68,69] To model defects at the InP surface, we perform calculations to obtain quasiparticle states of InAs/InP QDs with a passivation ligand pseudopotential removed from a single surface phosphorus atom, creating the equivalent of a phosphorus dangling bond.[70] We find that the unpassivated phosphorus atom creates a localized midgap quasiparticle state with an energy level between 200 and 500 meV above the quasiparticle valence band maximum (VBM) that depends on the specific location of the defect. Midgap states are not observed with the removal of a passivation ligand pseudopotential from an indium atom due to the relatively small electron effective mass. This finding is corroborated by the prior experimental work that has shown phosphorus dangling bonds formed through InP surface oxidation are responsible for deep trap states while unpassivated indium surface defects result in shallower midgap states.[68,69] The directional delocalization of the VBM state extends far into the InP shell and has a density overlap with InP surface trap states on the (111) face. While the introduction of a phosphorus dangling bond does not change the energy of the VBM, significant trap-VBM density overlaps may promote phonon-mediated trapping of holes at the valence band edge, leading to quenching of luminescence. Examples of facet-dependent defect impacts on the QD's VBM are shown in Figures 5 and S16 with trap locations, trap state energy levels, and density overlaps between the trap and VBM states reported in Tables S3 and S4.

As expected, we find that when the trap state is aligned with the lobes of the VBM density in the shell, the VBM has an increased localized density near the unpassivated phosphorus atom. Even with thin (e.g., 1.1 nm) InP shells, there is almost no overlap between the trap state and the VBM when it is located away from the (111) facets. As the InP shell thickness increases, the hole density in the shell increases, but the density overlap between the defect state and the VBM decreases. Across all InP thicknesses, defects located directly along the (111) axis present the greatest defect site-VBM overlap. To quantify the effect of the dangling bond on the VBM, we computed the overlap between the quasiparticle densities of the localized trap and the VBM. These values are shown in Table S2 and demonstrate that a dangling bond on the InP shell at the (111) surface can create a localized trap state that has a relatively large density overlap with the VBM, facilitating trapping of carriers to the surface and thereby decreasing PLQY. Thus, it is important to continue to improve development of particles with thick, uniform, protective ZnSe shells to prevent InP surface defects from quenching QD luminescence.

Based on the decreased overlap between surface defects and the VBM with increased InP shell thickness, we compare the exciton lifetimes between InAs/InP/ZnSe QDs with different InP thicknesses. As shown previously in Figure S4, the luminescence for thick InP (1.5 ± 0.1 nm)-shelled InAs/InP/ZnSe QDs can be improved from 1 to 51 ± 3% by better passivating the surface with more uniform and thicker (3 ML) ZnSe shells. We compare a pair of QDs with nearly identical InAs cores and ZnSe shells, with 1.0 ± 0.1 and 1.5 ± 0.1 nm thick InP shells. The PLQY for the compared samples are 55 ± 2 and 51 ± 3% respectively, enabling a more direct probe of the radiative lifetimes across the InP shell thickness since the QDs share similarly bright emission. Generally, there is a correlation between higher quality, defect-free materials with higher PLQY, and longer radiative lifetimes. Thus, reduction of the overlap between surface defects and the VBM from thicker InP shells may be expected to reduce hole trapping by surface

https://doi.org/10.1021/acs.jpcc.2c01499
J. Phys. Chem. C 2022, 126, 7576−7587

defects and extend exciton lifetimes. However, as shown in Figure 6a, we observe the exciton decay times to be 17.1 ± 0.1 and 11 ± 1 ns, respectively, for the 1.0 ± 0.1 and 1.5 ± 0.1 nm thick InP-shelled QDs, indicating that exciton lifetimes decrease with increased InP shell thickness.

Despite the expected decreased exciton trapping in the thicker-shelled InP QDs, the decreasing trend between the lifetime and shell thickness is attributed to the fact that the radiative lifetime depends on both the energy, ω, and the dipole moment, μ, of the transition according to

$$\tau_r = \frac{3\pi\varepsilon_0\hbar c^3}{\omega^3 |\mu|^2}$$

The optical gap of InAs/InP/ZnSe QDs depends on both the core size and shell thickness and decreases with both increasing InAs core diameter and InP shell thickness. While the size of the core is the primary component of the QD that dictates the optical gap, the InP shell thickness also plays a notable role. The prior work suggests a decrease in the fundamental gap between bare 3.4 nm InAs and the same QDs with 2 nm InP shells of up to 200 meV.[20] This is corroborated by both our experimental work and calculations, as illustrated in Figure S17. On the other hand, the transition dipole moment of the ground state exciton increases with increasing InAs and InP sizes, a trend that has been previously observed in other CdSe and InAs QD systems.[71−73] Together, the radiative lifetime depends inversely on the square of the transition dipole moment and inversely to the cube of the transition energy. Therefore, the radiative lifetime could increase or decrease with increasing shell thickness, depending on the rate of change of these properties with shell thickness for the specific material. As illustrated in Figure S17, the transition energy weakly decreases with increasing InP shell thickness while the transition dipole moment increases significantly with increasing InP shell thickness, causing the radiative lifetime to decrease with increasing InP shell thickness. These trends may not hold for CdSe/CdS,[74] in which excitons are significantly less quantum confined than they are in InAs/InP, explaining the discrepancy in results. Figure 6b depicts the combined effects of a decreasing optical gap and increasing dipole moment across particle sizes and shows the radiative lifetimes decrease with increasing InP shell thickness. Therefore, even though there may be reduced exciton trapping in thicker-shelled InP systems, suggesting improved surface passivation, the radiative lifetimes for excitons in InAs/InP/ZnSe QDs still decreases with thicker InP shells.

InAs core/multishell QDs offer exceptional promise for LSCs due to opportunities to tune the Stokes ratio and improve PLQY while retaining narrow emission. However, the current assessment of exciton lifetimes highlights the challenges in the development of highly luminescent InAs/InP/ZnSe QDs, especially if phosphorus dangling bonds are unavoidable. On one hand, it is important to increase the thickness of the InP shell to increase the Stokes ratio and decrease hole trapping. On the other hand, charge carriers delocalize to the shell more in systems with thicker InP shells, leading to greater opportunities for nonradiative losses as luminescence is highly sensitive to InP surface/interfacial defects. Thus, improvements to NIR emissive InAs/InP/ZnSe necessitate the highest quality and uniform ZnSe shell encapsulation for thick-shelled InP QDs. While this is challenged synthetically due to the slightly anisotropic InAs/InP structure, the synthetic procedures adopted here have proven to be adaptable to independent size modulation of the core and both shells to facilitate growth of several monolayer thick passivating ZnSe layers on large Stokes ratio particles (i.e., thick InP layers) to enhance luminescence. Growth of extremely thick ZnSe shells (>5 ML) in these systems, however, remains an unresolved synthetic challenge needing redress in future research. The scale of the challenge is well suggested by the past work. Near-unity CdSe/CdS QDs, for example, were prepared with 8 ML thick CdS shells,[41] suggesting that further material development to obtain thicker, uniform ZnSe shells may yield enhancements of emission and stability for the InAs/InP/ZnSe system as well.

CONCLUSIONS

This work highlights the need for materials with bright, NIR emissive luminophores with large Stokes ratios and narrow emission FWHM. We designed improvements for the synthesis of InAs/InP/ZnSe QDs that enable heavy metal-free, tunable, NIR emitters with 60 ± 2% PLQY, larger Stokes ratios, and narrow emission linewidths. While the NIR emitters reported here are among the brightest, cadmium-free InAs emitters with larger Stokes ratios, there are still synthetic and material challenges that must be addressed to realize high-performance LSCs and other NIR technologies. A primary reason for this challenge is attributed to the significant charge carrier occupation of the InP shell due to the strong quantum confinement of carriers in these structures, complicating the type I bulk alignment expected from bulk band gaps. Furthermore, defects at the InP/ZnSe interface, especially along the (111) facets, and unpassivated phosphorus dangling bonds lead to localized, deep trap states that have large density overlaps with the QD valence band maximum. These defects facilitate carrier trapping and decrease PLQY. Luminescence in InAs/InP/ZnSe is extremely sensitive to the quality of surface passivation. While our synthetic approach enables >50% PLQY NIR emitters, there remain opportunities for further development of InAs heterostructure QD systems to maximize their utility and realize LSC technologies.

ASSOCIATED CONTENT

Supporting Information

The Supporting Information is available free of charge at https://pubs.acs.org/doi/10.1021/acs.jpcc.2c01499.

Additional simulation details; method validation; additional transmission electron micrographs; absorption and emission spectra; elemental characterization; X-ray diffraction characterization; additional charge carrier density projections; and assessments of optical gaps and the transition dipole moment of QDs (PDF)

AUTHOR INFORMATION

Corresponding Author

Michael J. Enright − *Department of Chemistry, University of Illinois at Urbana Champaign, Urbana, Illinois 61801, United States; Department of Chemistry, Western Washington University, Bellingham, Washington 98225, United States;* orcid.org/0000-0003-1157-1741; Email: enright@wwu.edu

https://doi.org/10.1021/acs.jpcc.2c01499
J. Phys. Chem. C 2022, 126, 7576−7587

Authors

Dipti Jasrasaria − *Department of Chemistry, University of California, Berkeley, California 94720, United States;* orcid.org/0000-0001-7632-6718

Mathilde M. Hanchard − *Department of Chemistry, University of Illinois at Urbana Champaign, Urbana, Illinois 61801, United States*

David R. Needell − *Department of Applied Physics and Materials Science, California Institute of Technology, Pasadena, California 91125, United States*

Megan E. Phelan − *Department of Applied Physics and Materials Science, California Institute of Technology, Pasadena, California 91125, United States;* orcid.org/0000-0002-4968-7128

Daniel Weinberg − *Department of Chemistry, University of California, Berkeley, California 94720, United States; Materials Sciences Division, Lawrence Berkeley National Laboratory, Berkeley, California 94720, United States;* orcid.org/0000-0001-7552-4712

Brinn E. McDowell − *Department of Chemistry, University of Illinois at Urbana Champaign, Urbana, Illinois 61801, United States*

Haw-Wen Hsiao − *Department of Materials Science and Engineering, University of Illinois at Urbana-Champaign, Urbana, Illinois 61801, United States*

Hamidreza Akbari − *Department of Applied Physics and Materials Science, California Institute of Technology, Pasadena, California 91125, United States;* orcid.org/0000-0002-6073-3885

Matthew Kottwitz − *Department of Chemistry, University of Illinois at Urbana Champaign, Urbana, Illinois 61801, United States*

Maggie M. Potter − *Department of Chemical and Biomolecular Engineering, University of Illinois at Urbana Champaign, Urbana, Illinois 61801, United States;* orcid.org/0000-0002-6262-1078

Joeson Wong − *Department of Applied Physics and Materials Science, California Institute of Technology, Pasadena, California 91125, United States;* orcid.org/0000-0002-6304-7602

Jian-Min Zuo − *Department of Materials Science and Engineering, University of Illinois at Urbana-Champaign, Urbana, Illinois 61801, United States;* orcid.org/0000-0002-5151-3370

Harry A. Atwater − *Department of Applied Physics and Materials Science, California Institute of Technology, Pasadena, California 91125, United States;* orcid.org/0000-0001-9435-0201

Eran Rabani − *Department of Chemistry, University of California, Berkeley, California 94720, United States; Materials Sciences Division, Lawrence Berkeley National Laboratory, Berkeley, California 94720, United States; The Sackler Center for Computational Molecular and Materials Science, Tel Aviv University, Tel Aviv 69978, Israel;* orcid.org/0000-0003-2031-3525

Ralph G. Nuzzo − *Department of Chemistry, University of Illinois at Urbana Champaign, Urbana, Illinois 61801, United States; Surface and Corrosion Science, School of Engineering Sciences in Chemistry, Biotechnology and Health, KTH Royal Institute of Technology, Stockholm 10044, Sweden*

Complete contact information is available at: https://pubs.acs.org/10.1021/acs.jpcc.2c01499

Author Contributions

Conceptualization: M.J.E., D.J., D.R.N., M.E.P., M.M.P., H.A.A., E.R., and R.G.N; methodology: M.J.E., D.J., D.R.N., and D.W; investigation: M.J.E., D.J., M.M.H., D.R.N., D.W., B.E.M., H.-W.H., and M.K.; resources: H.A.A., E.R., and R.G.N; writing: M.J.E. and D.J.; review and editing: M.E.P., H.A., M.M.P., and J.W; supervision: M.J.E., J.-M.Z., H.A.A., E.R., and R.G.N.; and funding acquisition: H.A.A., E.R., and R.G.N. The manuscript was written through contributions of all authors. All authors have given approval to the final version of the manuscript.

Notes

The authors declare no competing financial interest.

■ ACKNOWLEDGMENTS

This work (material synthesis, modeling, and characterization) has been primarily supported by the Photonics at Thermodynamic Limits Energy Frontier Research Center funded by the U.S. Department of Energy, Office of Science, and Office of Basic Energy Sciences under Award Number DE-SC0019140. Synthesis and characterization of materials was carried out in part in the Illinois Materials Research Laboratory Central Research Facilities, University of Illinois. The authors would like to thank Julio Soares for assistance with time-resolved photoluminescence measurements and analysis and Danielle Gray for fruitful discussions on sample digestion for ICP−OES. D.J. acknowledges the support of the Computational Science Graduate Fellowship from the U.S. Department of Energy under Grant No. DE-SC0019323.

■ REFERENCES

(1) Steckel, J. S.; Coe-Sullivan, S.; Bulović, V.; Bawendi, M. G. 1.3μm to 1.55μm Tunable Electroluminescence from PbSe Quantum Dots Embedded within an Organic Device. *Adv. Mater.* **2003**, *15*, 1862−1866.

(2) Konstantatos, G.; Howard, I.; Fischer, A.; Hoogland, S.; Clifford, J.; Klem, E.; Levina, L.; Sargent, E. H. Ultrasensitive Solution-Cast Quantum Dot Photodetectors. *Nature* **2006**, *442*, 180−183.

(3) Sun, Q.; Wang, Y. A.; Li, L. S.; Wang, D.; Zhu, T.; Xu, J.; Yang, C.; Li, Y. Bright, Multicoloured Light-Emitting Diodes Based on Quantum Dots. *Nat. Photonics* **2007**, *1*, 717−722.

(4) Nozik, A. J.; Beard, M. C.; Luther, J. M.; Law, M.; Ellingson, R. J.; Johnson, J. C. Semiconductor Quantum Dots and Quantum Dot Arrays and Applications of Multiple Exciton Generation to Third-Generation Photovoltaic Solar Cells. *Chem. Rev.* **2010**, *110*, 6873−6890.

(5) Keuleyan, S.; Lhuillier, E.; Brajuskovic, V.; Guyot-Sionnest, P. Mid-Infrared HgTe Colloidal Quantum Dot Photodetectors. *Nat. Photonics* **2011**, *5*, 489−493.

(6) Dai, X.; Zhang, Z.; Jin, Y.; Niu, Y.; Cao, H.; Liang, X.; Chen, L.; Wang, J.; Peng, X. Solution-Processed, High-Performance Light-Emitting Diodes Based on Quantum Dots. *Nature* **2014**, *515*, 96−99.

(7) Carey, G. H.; Abdelhady, A. L.; Ning, Z.; Thon, S. M.; Bakr, O. M.; Sargent, E. H. Colloidal Quantum Dot Solar Cells. *Chem. Rev.* **2015**, *115*, 12732−12763.

(8) Lu, H.; Carroll, G. M.; Neale, N. R.; Beard, M. C. Infrared Quantum Dots: Progress, Challenges, and Opportunities. *ACS Nano* **2019**, *13*, 939−953.

(9) Klem, E. J. D.; Levina, L.; Sargent, E. H. PbS Quantum Dot Electroabsorption Modulation across the Extended Communications Band 1200−1700 Nm. *Appl. Phys. Lett.* **2005**, *87*, No. 053101.

(10) Sargent, E. H. Solution-Processed Infrared Optoelectronics: Photovoltaics, Sensors, and Sources. *IEEE J. Sel. Top. Quantum Electron.* **2008**, *14*, 1223−1229.
(11) Bruns, O. T.; Bischof, T. S.; Harris, D. K.; Franke, D.; Shi, Y.; Riedemann, L.; Bartelt, A.; Jaworski, F. B.; Carr, J. A.; Rowlands, C. J.; et al. Next-Generation in Vivo Optical Imaging with Short-Wave Infrared Quantum Dots. *Nat. Biomed. Eng.* **2017**, *1*, No. 0056.
(12) Meinardi, F.; McDaniel, H.; Carulli, F.; Colombo, A.; Velizhanin, K. A.; Makarov, N. S.; Simonutti, R.; Klimov, V. I.; Brovelli, S. Highly Efficient Large-Area Colourless Luminescent Solar Concentrators Using Heavy-Metal-Free Colloidal Quantum Dots. *Nat. Nanotechnol.* **2015**, *10*, 878−885.
(13) Sargent, E. H. Infrared Quantum Dots. *Adv. Mater.* **2005**, *17*, 515−522.
(14) Ma, Q.; Su, X. Near-Infrared Quantum Dots: Synthesis, Functionalization and Analytical Applications. *Analyst* **2010**, *135*, 1867−1877.
(15) Kershaw, S. V.; Susha, A. S.; Rogach, A. L. Narrow Bandgap Colloidal Metal Chalcogenide Quantum Dots: Synthetic Methods, Heterostructures, Assemblies, Electronic and Infrared Optical Properties. *Chem. Soc. Rev.* **2013**, *42*, 3033−3087.
(16) Colvin, V. L.; Schlamp, M. C.; Alivisatos, A. P. Light-Emitting Diodes Made from Cadmium Selenide Nanocrystals and a Semiconducting Polymer. *Nature* **1994**, *370*, 354−357.
(17) Dabbousi, B. O.; Bawendi, M. G.; Onitsuka, O.; Rubner, M. F. Electroluminescence from CdSe Quantum-Dot/Polymer Composites. *Appl. Phys. Lett.* **1995**, *66*, 1316.
(18) Mattoussi, H.; Radzilowski, L. H.; Dabbousi, B. O.; Thomas, E. L.; Bawendi, M. G.; Rubner, M. F. Electroluminescence from Heterostructures of Poly(Phenylene Vinylene) and Inorganic CdSe Nanocrystals. *J. Appl. Phys.* **1998**, *83*, 7965−7974.
(19) Schlamp, M. C.; Peng, X.; Alivisatos, A. P. Improved Efficiencies in Light Emitting Diodes Made with CdSe(CdS) Core/Shell Type Nanocrystals and a Semiconducting Polymer. *J. Appl. Phys.* **1997**, *82*, 5837−5842.
(20) Cao, Y. W.; Banin, U. Growth and Properties of Semiconductor Core/Shell Nanocrystals with InAs Cores. *J. Am. Chem. Soc.* **2000**, *122*, 9692−9702.
(21) Bruchez, M.; Moronne, M.; Gin, P.; Weiss, S.; Alivisatos, A. P. Semiconductor Nanocrystals as Fluorescent Biological Labels. *Science* **1998**, *281*, 2013−2016.
(22) Mitchell, G. P.; Mirkin, C. A.; Letsinger, R. L. Programmed Assembly of DNA Functionalized Quantum Dots [10]. *J. Am. Chem. Soc.* **1999**, *121*, 8122−8123.
(23) Chan, W. C. W.; Nie, S. Quantum Dot Bioconjugates for Ultrasensitive Nonisotopic Detection. *Science* **1998**, *281*, 2016−2018.
(24) Bradshaw, L. R.; Knowles, K. E.; McDowall, S.; Gamelin, D. R. Nanocrystals for Luminescent Solar Concentrators. *Nano Lett.* **2015**, *15*, 1315−1323.
(25) Meinardi, F.; Colombo, A.; Velizhanin, K. A.; Simonutti, R.; Lorenzon, M.; Beverina, L.; Viswanatha, R.; Klimov, V. I.; Brovelli, S. Large-Area Luminescent Solar Concentrators Based on Stokes-Shift-Engineered Nanocrystals in a Mass-Polymerized PMMA Matrix. *Nat. Photonics* **2014**, *8*, 392−399.
(26) Goetzberger, A.; Greube, W. Solar Energy Conversion with Fluorescent Collectors. *Appl. Phys.* **1977**, *14*, 123−139.
(27) Naczynski, D. J.; Tan, M. C.; Zevon, M.; Wall, B.; Kohl, J.; Kulesa, A.; Chen, S.; Roth, C. M.; Riman, R. E.; Moghe, P. V. Rare-Earth-Doped Biological Composites as in Vivo Shortwave Infrared Reporters. *Nat. Commun.* **2013**, *4*, No. 2199.
(28) Wang, R.; Li, X.; Zhou, L.; Zhang, F. Epitaxial Seeded Growth of Rare-Earth Nanocrystals with Efficient 800 Nm Near-Infrared to 1525 Nm Short-Wavelength Infrared Downconversion Photoluminescence for In Vivo Bioimaging. *Angew. Chem., Int. Ed.* **2014**, *53*, 12086−12090.
(29) Zhang, Y.; Hong, G.; Zhang, Y.; Chen, G.; Li, F.; Dai, H.; Wang, Q. Ag 2S Quantum Dot: A Bright and Biocompatible Fluorescent Nanoprobe in the Second near-Infrared Window. *ACS Nano* **2012**, *6*, 3695−3702.
(30) Hatami, S.; Würth, C.; Kaiser, M.; Leubner, S.; Gabriel, S.; Bahrig, L.; Lesnyak, V.; Pauli, J.; Gaponik, N.; Eychmüller, A.; et al. Absolute Photoluminescence Quantum Yields of IR26 and IR-Emissive Cd1-XHgxTe and PbS Quantum Dots-Method- and Material-Inherent Challenges. *Nanoscale* **2015**, *7*, 133−143.
(31) Semonin, O. E.; Johnson, J. C.; Luther, J. M.; Midgett, A. G.; Nozik, A. J.; Beard, M. C. Absolute Photoluminescence Quantum Yields of IR-26 Dye, PbS, and PbSe Quantum Dots. *J. Phys. Chem. Lett.* **2010**, *1*, 2445−2450.
(32) Rurack, K.; Spieles, M. Fluorescence Quantum Yields of a Series of Red and Near-Infrared Dyes Emitting at 600-1000 Nm. *Anal. Chem.* **2011**, *83*, 1232−1242.
(33) Srivastava, V.; Kamysbayev, V.; Hong, L.; Dunietz, E.; Klie, R. F.; Talapin, D. V. Colloidal Chemistry in Molten Salts: Synthesis of Luminescent In1- XGaxP and In1- XGaxAs Quantum Dots. *J. Am. Chem. Soc.* **2018**, *140*, 12144−12151.
(34) Sagar, L. K.; Bappi, G.; Johnston, A.; Chen, B.; Todorović, P.; Levina, L.; Saidaminov, M. I.; García de Arquer, F. P.; Hoogland, S.; Sargent, E. H. Single-Precursor Intermediate Shelling Enables Bright, Narrow Line Width InAs/InZnP-Based QD Emitters. *Chem. Mater.* **2020**, *32*, 2919−2925.
(35) Reiss, P.; Protière, M.; Li, L. Core/Shell Semiconductor Nanocrystals. *Small* **2009**, *5*, 154−168.
(36) Franke, D.; Harris, D. K.; Chen, O.; Bruns, O. T.; Carr, J. A.; Wilson, M. W. B.; Bawendi, M. G. Continuous Injection Synthesis of Indium Arsenide Quantum Dots Emissive in the Short-Wavelength Infrared. *Nat. Commun.* **2016**, *7*, No. 12749.
(37) Aharoni, A.; Mokari, T.; Popov, I.; Banin, U. Synthesis of InAs/CdSe/ZnSe Core/Shell1/Shell2 Structures with Bright and Stable near-Infrared Fluorescence. *J. Am. Chem. Soc.* **2006**, *128*, 257−264.
(38) Enright, M. J.; Dou, F. Y.; Wu, S.; Rabe, E. J.; Monahan, M.; Friedfeld, M. R.; Schlenker, C. W.; Cossairt, B. M. Seeded Growth of Nanoscale Semiconductor Tetrapods: Generality and the Role of Cation Exchange. *Chem. Mater.* **2020**, *32*, 4774−4784.
(39) Stein, J. L.; Steimle, M. I.; Terban, M. W.; Petrone, A.; Billinge, S. J. L.; Li, X.; Cossairt, B. M. Cation Exchange Induced Transformation of InP Magic-Sized Clusters. *Chem. Mater.* **2017**, *29*, 7984−7992.
(40) Bronstein, N. D.; Yao, Y.; Xu, L.; O'Brien, E.; Powers, A. S.; Ferry, V. E.; Alivisatos, A. P.; Nuzzo, R. G. Quantum Dot Luminescent Concentrator Cavity Exhibiting 30-fold Concentration. *ACS Photonics* **2015**, *2* (11), 1576−1583.
(41) Hanifi, D. A.; Bronstein, N. D.; Koscher, B. A.; Nett, Z.; Swabeck, J. K.; Takano, K.; Schwartzberg, A. M.; Maserati, L.; Vandewal, K.; van de Burgt, Y.; et al. Redefining Near-Unity Luminescence in Quantum Dots with Photothermal Threshold Quantum Yield. *Science* **2019**, *363*, 1199−1202.
(42) Bauser, H. C.; Bukowsky, C. R.; Phelan, M.; Weigand, W.; Needell, D. R.; Holman, Z. C.; Atwater, H. A. Photonic Crystal Waveguides for>90% Light Trapping Efficiency in Luminescent Solar Concentrators. *ACS Photonics* **2020**, *7*, 2122−2131.
(43) Li, Y.; Hou, X.; Dai, X.; Yao, Z.; Lv, L.; Jin, Y.; Peng, X. Stoichiometry-Controlled InP-Based Quantum Dots: Synthesis, Photoluminescence, and Electroluminescence. *J. Am. Chem. Soc.* **2019**, *141*, 6448−6452.
(44) Pietra, F.; Kirkwood, N.; De Trizio, L.; Hoekstra, A. W.; Kleibergen, L.; Renaud, N.; Koole, R.; Baesjou, P.; Manna, L.; Houtepen, A. J. Ga for Zn Cation Exchange Allows for Highly Luminescent and Photostable InZnP-Based Quantum Dots. *Chem. Mater.* **2017**, *29*, 5192−5199.
(45) Kim, S.; Kim, T.; Kang, M.; Kwak, S. K.; Yoo, T. W.; Park, L. S.; Yang, I.; Hwang, S.; Lee, J. E.; Kim, S. K.; et al. Highly Luminescent InP/GaP/ZnS Nanocrystals and Their Application to White Light-Emitting Diodes. *J. Am. Chem. Soc.* **2012**, *134*, 3804−3809.
(46) Wijaya, H.; Darwan, D.; Lim, K. R. G.; Wang, T.; Khoo, K. H.; Tan, Z. K. Large-Stokes-Shifted Infrared-Emitting InAs-In(Zn)P-ZnSe-ZnS Giant-Shell Quantum Dots by One-Pot Continuous-Injection Synthesis. *Chem. Mater.* **2019**, *31*, 2019−2026.

https://doi.org/10.1021/acs.jpcc.2c01499
J. Phys. Chem. C 2022, 126, 7576−7587

(47) Wijaya, H.; Darwan, D.; Zhao, X.; Woan Yuann Ong, E.; Rui Garrick Lim, K.; Wang, T.; Jun Lim, L.; Hong Khoo, K.; Tan, Z.-K.; Wijaya, H.; et al. Efficient Near-Infrared Light-Emitting Diodes Based on In(Zn)As−In(Zn)P−GaP−ZnS Quantum Dots. *Adv. Funct. Mater.* **2020**, *30*, No. 1906483.
(48) Xie, R.; Chen, K.; Chen, X.; Peng, X. InAs/InP/ZnSe Core/Shell/Shell Quantum Dots as near-Infrared Emitters: Bright, Narrow-Band, Non-Cadmium Containing, and Biocompatible. *Nano Res.* **2008**, *1*, 457−464.
(49) Wells, R. L.; Self, M. F.; Johansen, J. D.; Laske, J. A.; Aubuchon, S. R.; Jones III, L. J.; Cowley, A. H.; Kamepalli, S. Tris-(Trimethylsilyl)Arsine and Lithium Bis(Trimethylsilyl)Arsenide. In *Inorganic Syntheses*; John Wiley & Sons, Inc., 1996; pp 150−158.
(50) Ginterseder, M.; Franke, D.; Perkinson, C. F.; Wang, L.; Hansen, E. C.; Bawendi, M. G. Scalable Synthesis of InAs Quantum Dots Mediated through Indium Redox Chemistry. *J. Am. Chem. Soc.* **2020**, *142*, 4088−4092.
(51) Şahin, D.; Ilan, B.; Kelley, D. F. Monte-Carlo Simulations of Light Propagation in Luminescent Solar Concentrators Based on Semiconductor Nanoparticles. *J. Appl. Phys.* **2011**, *110*, No. 033108.
(52) Kennedy, M.; McCormack, S. J.; Doran, J.; Norton, B. Ray-Trace Modelling of Reflectors for Quantum Dot Solar Concentrators. In *High and Low Concentration for Solar Electric Applications II*; Symko-Davies, M., Ed.; Society of Photo Optical, 2007; Vol. *6649*, p 664905.
(53) Williamson, A.; Zunger, A. Pseudopotential Study of Electron-Hole Excitations in Colloidal Free-Standing InAs Quantum Dots. *Phys. Rev. B* **2000**, *61*, 1978−1991.
(54) Fu, H.; Zunger, A. Local-Density-Derived Semiempirical Nonlocal Pseudopotentials for InP with Applications to Large Quantum Dots. *Phys. Rev. B* **1997**, *55*, 1642.
(55) Rabani, E.; Hetényi, B.; Berne, B. J.; Brus, L. E. Electronic Properties of CdSe Nanocrystals in the Absence and Presence of a Dielectric Medium. *J. Chem. Phys.* **1999**, *110*, 5355−5369.
(56) Philbin, J. P.; Rabani, E. Electron-Hole Correlations Govern Auger Recombination in Nanostructures. *Nano Lett.* **2018**, *18*, 7889−7895.
(57) Han, P.; Bester, G. Interatomic Potentials for the Vibrational Properties of III-V Semiconductor Nanostructures. *Phys. Rev. B* **2011**, *83*, No. 174304.
(58) Plimpton, S. Fast Parallel Algorithms for Short-Range Molecular Dynamics. *J. Comput. Phys.* **1995**, *117*, 1−19.
(59) Mundy, M. E.; Eagle, F. W.; Hughes, K. E.; Gamelin, D. R.; Cossairt, B. M. Synthesis and Spectroscopy of Emissive, Surface-Modified, Copper-Doped Indium Phosphide Nanocrystals. *ACS Mater. Lett.* **2020**, *2*, 576−581.
(60) Park, J.; Won, Y.-H.; Han, Y.; Kim, H.-M.; Jang, E.; Kim, D.; Park, J.; Kim, D.; Won, Y.-H.; Han, Y.; et al. Tuning Hot Carrier Dynamics of InP/ZnSe/ZnS Quantum Dots by Shell Morphology Control. *Small* **2021**, *18*, No. 2105492.
(61) Sagar, L. K.; Bappi, G.; Johnston, A.; Chen, B.; Todorović, P.; Levina, L.; Saidaminov, M. I.; García De Arquer, F. P.; Nam, D. H.; Choi, M. J.; et al. Suppression of Auger Recombination by Gradient Alloying in InAs/CdSe/CdS QDs. *Chem. Mater.* **2020**, *32*, 7703−7709.
(62) Fu, H.; Zunger, A. InP Quantum Dots: Electronic Structure, Surface Effects, and the Redshifted Emission. *Phys. Rev. B* **1997**, *56*, 1496−1508.
(63) Wei, S. H.; Zunger, A. Calculated Natural Band Offsets of All II-VI and III-V Semiconductors: Chemical Trends and the Role of Cation d Orbitals. *Appl. Phys. Lett.* **1998**, *72*, 2011−2013.
(64) Mushonga, P.; Onani, M. O.; Madiehe, A. M.; Meyer, M. Indium Phosphide-Based Semiconductor Nanocrystals and Their Applications. *J. Nanomater.* **2012**, *2012*, No. 12.
(65) Gong, M.; Duan, K.; Li, C. F.; Magri, R.; Narvaez, G. A.; He, L. Electronic Structure of Self-Assembled InAs InP Quantum Dots: Comparison with Self-Assembled InAs GaAs Quantum Dots. *Phys. Rev. B* **2008**, *77*, No. 045326.
(66) Li, Y. H.; Gong, X. G.; Wei, S. H. Ab Initio All-Electron Calculation of Absolute Volume Deformation Potentials of IV-IV, III-V, and II-VI Semiconductors: The Chemical Trends. *Phys. Rev. B* **2006**, *73*, No. 245206.
(67) Won, Y. H.; Cho, O.; Kim, T.; Chung, D. Y.; Kim, T.; Chung, H.; Jang, H.; Lee, J.; Kim, D.; Jang, E. Highly Efficient and Stable InP/ZnSe/ZnS Quantum Dot Light-Emitting Diodes. *Nature* **2019**, *575*, 634−638.
(68) Stein, J. L.; Holden, W. M.; Venkatesh, A.; Mundy, M. E.; Rossini, A. J.; Seidler, G. T.; Cossairt, B. M. Probing Surface Defects of InP Quantum Dots Using Phosphorus Kα and Kβ X-Ray Emission Spectroscopy. *Chem. Mater.* **2018**, *30*, 6377−6388.
(69) Kim, Y.; Chang, J. H.; Choi, H.; Kim, Y. H.; Bae, W. K.; Jeong, S. III-V Colloidal Nanocrystals: Control of Covalent Surfaces. *Chem. Sci.* **2020**, *11*, 913−922.
(70) Jasrasaria, D.; Philbin, J. P.; Yan, C.; Weinberg, D.; Alivisatos, A. P.; Rabani, E. Sub-Bandgap Photoinduced Transient Absorption Features in CdSe Nanostructures: The Role of Trapped Holes. *J. Phys. Chem. C* **2020**, *124*, 17372−17378.
(71) Leatherdale, C. A.; Woo, W. K.; Mikulec, F. V.; Bawendi, M. G. On the Absorption Cross Section of CdSe Nanocrystal Quantum Dots. *J. Phys. Chem. B* **2002**, *106*, 7619−7622.
(72) Jasieniak, J.; Smith, L.; Van Embden, J.; Mulvaney, P.; Califano, M. Re-Examination of the Size-Dependent Absorption Properties of CdSe Quantum Dots. *J. Phys. Chem. C* **2009**, *113*, 19468−19474.
(73) Yu, P.; Beard, M. C.; Ellingson, R. J.; Fernere, S.; Curtis, C.; Drexler, J.; Luiszer, F.; Nozik, A. J. Absorption Cross-Section and Related Optical Properties of Colloidal InAs Quantum Dots. *J. Phys. Chem. B* **2005**, *109*, 7084−7087.
(74) Pu, C.; Peng, X. To Battle Surface Traps on CdSe/CdS Core/Shell Nanocrystals: Shell Isolation versus Surface Treatment. *J. Am. Chem. Soc.* **2016**, *138*, 8134−8142.

https://doi.org/10.1021/acs.jpcc.2c01499
J. Phys. Chem. C 2022, 126, 7576−7587